Research Square

Preprints are preliminary reports that have not undergone peer review.
They should not be considered conclusive, used to inform clinical practice,
or referenced by the media as validated information.

Improving Magnetic Bead-Based Nucleic Acid Extraction by Modulating Acoustic Streaming Configuration

yuan qian
Xiamen University
Jiayu Yang
Xiamen University
Lili Pan
Xiamen University
Ran An
Xiamen University
Zhuolun Li
Xiamen University
Yuhong Yang
Xiamen University
Junnan Wang
Xiamen University
Lin Xiao
Xiamen University
Tiesheng Zheng
Xiamen University
Ningshao Xia
Xiamen University
Fa Zhang
Xiamen University
Lijie Yuan
Xiamen Medical College
Dongxu Zhang
zhangdongxu@xmu.edu.cn

Xiamen University

Research Article

Keywords: Acoustic streaming configuration, Magnetic bead transport, Nucleic acid extraction, Ultrasound-assisted sample preparation, Serum matrix

Posted Date: November 18th, 2026

DOI: https://doi.org/10.21203/rs.3.rs-11377238/v1

License: This work is licensed under a Creative Commons Attribution 4.0 International License. Read Full License

Additional Declarations: No competing interests reported.

Abstract

Efficient magnetic bead-based nucleic acid extraction (NAE) requires fluid motion that supports bead resuspension and redistribution within confined reaction volumes. Here, we investigated acoustic streaming configuration as a design variable in an externally actuated, closed polypropylene chamber containing a 205 μL reaction mixture. Four configurations were generated by varying the ultrasound incidence angle while maintaining the same nominal driving power, frequency, and contact force. We used multi-descriptor characterization and joint interpretation to relate simulated acoustic streaming and bead transport to independently measured qPCR responses. The descriptors distinguished local flow intensity from spatial coverage and population-level bead displacement from internal rearrangement. High-speed images provided qualitative observations of bead redistribution. Although the 0° configuration produced the highest simulated local peak velocity, the 10° configuration provided broader effective streaming coverage and greater bead redistribution. In HCMV-spiked fetal bovine serum, the 10° configuration yielded a mean Ct of 30.86 ± 0.28, compared with 31.38 ± 0.19 at 0° and 31.87 ± 0.27 for manual extraction. Each condition comprised three independent extractions, each analyzed in three technical qPCR replicates; the reported means and standard deviations were calculated from the three extraction-level mean Ct values. Assuming 100% qPCR amplification efficiency, the estimated relative target yield at 10° was 2.02 times that of manual extraction. No amplification was observed in extraction blanks or no-template controls. These findings support considering streaming coverage and the resulting bead transport alongside local velocity magnitude when optimizing ultrasound-assisted magnetic bead extraction.

1. Introduction

Mixing is an important operation in chemical reactions, biological sample preparation, and particle-based separation processes[1–3], where it promotes reagent distribution and contact between interacting components[4–6]. In confined reaction chambers containing suspended particles, effective mixing involves both liquid redistribution and particle transport[7–9]. Strong local fluid motion may coexist with limited circulation elsewhere, while particle sedimentation or localized accumulation may restrict contact with the surrounding liquid[10–12]. Assessing mixing conditions therefore requires consideration of the spatial extent of flow and the resulting particle motion, in addition to local flow intensity[13–15]. This makes flow configuration, including the spatial distribution of fluid motion and circulation pathways, an important consideration in the design of compact sample-preparation systems.

Magnetic bead-based nucleic acid extraction (NAE) is a representative application in which liquid mixing and particle transport must be considered together. As a critical sample-preparation step in molecular diagnostics, NAE affects the sensitivity and reproducibility of downstream PCR, sequencing, and other nucleic acid assays[16–18]. Mixing promotes contact between biological samples and lysis reagents and redistributes magnetic beads for the capture of released nucleic acids. Although magnetic bead-based extraction is well suited to automated and closed systems, bead sedimentation or localized accumulation can limit bead distribution and opportunities for bead–target contact[19, 20]. Pipetting and

vortex mixing can alleviate these limitations, but integrating these operations into compact closed systems can require additional mechanical components. Acoustic actuation offers an alternative means of generating fluid motion and mobilizing beads, motivating investigation of how the resulting streaming configurations and bead-transport characteristics relate to extraction outcomes[21, 22].

Acoustofluidic actuation provides a compact means of generating fluid motion and particle transport without repeated mechanical access to the reaction chamber. Depending on the acoustic mode and device structure, ultrasound can induce acoustic streaming[23], acoustic radiation forces[24], local shear, and cavitation-related effects[25, 26]. Acoustic streaming is particularly relevant to mixing because it converts oscillatory acoustic excitation into time-averaged circulation, which can shorten transport distances, accelerate fluid exchange, and exert drag on suspended particles. Surface acoustic waves, bulk acoustic waves, oscillating bubbles, sharp-edge structures, and localized resonators have consequently been used for micromixing, pumping, particle focusing, trapping, cell manipulation, and bead resuspension[27–29]. These studies establish acoustic streaming as a versatile mechanism for coupled fluid and particle manipulation in confined systems, providing a physical basis for its application to magnetic bead-based NAE. Previous studies have demonstrated the feasibility of using acoustic streaming for sample preparation and NAE. Iranmanesh[30] et al. generated high-velocity acoustic micro-vortexing in a disposable polymer chip containing a 20 μL chamber, enabling rapid fluid mixing, resuspension of magnetically collected beads, and cell lysis followed by DNA extraction within 25 s. More recently, Li [31]et al. developed reconfigurable acoustic streaming tweezers based on two GHz solid-mounted resonators. By switching between particle-separation and vortex-mixing modes, their system performed automated NAE from 10–400 μL samples and was validated using buffer, serum, and whole-blood matrices. These studies show that acoustic streaming can support both magnetic bead manipulation and nucleic acid extraction and that it can be extended from proof-of-concept microfluidic samples to complex biological matrices.

These studies motivate a further question: which features of acoustic streaming and bead transport are associated with improved extraction outcomes in a given chamber? Demonstrating the presence of acoustic mixing does not by itself identify which spatial flow characteristics are favorable for extraction. Acoustic streaming is spatially nonuniform and is strongly influenced by chamber geometry, actuator position, coupling orientation, boundary conditions, and operating mode. Consequently, two configurations operated at the same nominal power may produce different vortex locations, circulation ranges, stagnant regions, and particle trajectories. A high local velocity may indicate strong actuation near the source but may not ensure that the flow reaches sedimented beads or renews bead–liquid contact throughout the chamber. Addressing this question requires distinguishing complementary aspects of transport. Local peak velocity and flow coverage describe different aspects of the streaming field, while centroid displacement and internal rearrangement distinguish collective translation from changes within the bead population. Their joint interpretation can reveal transport differences that are obscured by a single summary value. Comparison with independently measured extraction outcomes can then identify both consistent associations and discrepancies.

Here, we investigated acoustic streaming configuration in an externally actuated, closed polypropylene chamber containing a 205 μL reaction mixture. Four incidence angles were compared while nominal driving power, frequency, contact force, and chamber geometry were maintained. Incidence angle served as a means of generating different acoustic and transport conditions. Multi-descriptor characterization was used to distinguish flow intensity and coverage, overall bead migration, internal rearrangement, and temporal redistribution. The image sequences provided qualitative context for bead redistribution. Extraction experiments using HCMV-spiked fetal bovine serum provided qPCR measurements for comparison with the simulated transport profiles. Joint interpretation examined both correspondence and discrepancies between the two types of evidence. The objective was to identify transport features relevant to configuration assessment within the tested chamber, rather than establish a universal incidence-angle optimum.

2. Materials and Methods

2.1 Preprocessing platform design

Disposable polypropylene (PP) chips were used as nucleic acid extraction chambers. PP is compatible with ISO 10993 biological evaluation requirements for medical devices and is widely used in commercial clinical diagnostic products. The reaction chamber had a quarter-spherical geometry, a curvature radius of 7 mm, a wall thickness of 1 mm, and an estimated volume of approximately 0.36 mL. The chamber was designed to accommodate the sample, lysis buffer, and magnetic bead suspension.

A six-degree-of-freedom motion-control system was developed to adjust the relative alignment between the ultrasonic transducer and the reaction chamber. The transducer was mounted on the motion platform, and the normal vector of its end face was constrained within the symmetry plane of the chamber and directed toward the geometric center of the spherical cavity. The angle between the transducer normal and the vertical axis was defined as the ultrasonic incidence angle θ. The angle could be adjusted from 0° to 40°, and 0°, 10°, 20°, and 30° were selected for evaluating magnetic bead dispersion and nucleic acid extraction. The transducer was coupled to the external chamber wall through a mechanical fixture and advanced by an electric cylinder. A force sensor monitored the contact state, and a PID control algorithm maintained the contact force at 10 N to reduce variations in ultrasonic transmission. The platform configuration is shown in Fig. 1.

2.2 Ultrasonic parameters and acoustic pressure assessment

The ultrasonic transducer operated at 39.8 kHz, which matched the modal response of the reaction chamber. At maximum driving power, the peak vibration amplitude at the transducer end face was approximately 15 μm. The driving power was nearly linearly correlated with the end-face amplitude. All ultrasound-assisted lysis experiments were performed for 10 s.

The acoustic pressure response in the reaction chamber was measured using a hydrophone (NH4000, Precision Acoustics Ltd.). The θ = 0° configuration was used as the reference condition during calibration. To reduce ambient noise and non-target frequency components, the acquired signals were band-pass filtered at 35–42 kHz before time-domain pressure analysis.

2.3 Computational modelling of acoustic and fluid dynamics

In the acoustic model, transducer excitation was simplified as a prescribed vibration boundary condition on the inner wall corresponding to the contact region. The displacement due to vibration at the transducer's end face is depicted as the sum of the elastic displacement induced by the contact force and the oscillatory vibration displacement, expressed as $\delta + A_0 \, sin\,(2\pi \, ft)$, where A_0 denotes the characteristic amplitude at maximum power, δ signifies the elastic displacement related to the contact force, and f represents the ultrasonic frequency. The contact-interface geometry was described using Hertz contact theory, and the relevant equations are provided in the **Supplementary Material**.

Deionized water was used as a simplified fluid medium for comparing acoustic and streaming fields across configurations. Differences between water and the extraction mixture may affect the quantitative predictions, so the simulations were interpreted primarily as comparative descriptions rather than exact reproductions of the extraction environment. The ratio of chamber-wall thickness h to acoustic wavelength λ was approximately 0.03, which is below the thin-wall approximation threshold of 0.1. The thin-wall assumption was therefore adopted. The governing equations, boundary conditions, and quantitative criteria for the acoustic and streaming fields are provided in the **Supplementary Material**.

2.4 Magnetic bead dynamics and dispersion modelling

Based on the acoustic and streaming fields, a Monte Carlo model was established to describe magnetic bead dispersion under ultrasonic actuation. The simulated magnetic beads had a diameter of 22 μm, consistent with the beads used in the extraction experiments. Before ultrasonic actuation, the beads were initialized at the bottom of the reaction chamber to mimic gravitational sedimentation before the experiment.

In the model, magnetic beads were treated as rigid spheres, the fluid was treated as Newtonian, and the streaming field was approximated as quasi-steady. Four forces were considered: acoustic radiation force, fluid drag, gravity, and buoyancy. Other hydrodynamic effects, such as the Magnus force, were neglected. Detailed parameters and computational procedures are provided in the Supplementary Material. Bead-wall interactions were treated as fully elastic collisions. The model describes bead transport and spatial redistribution rather than interparticle aggregation or aggregate breakup. Redistribution was quantified using the metrics described in the **Supplementary Material**.

Magnetic bead motion was recorded using a high-speed microscopic imaging system (Fastcam Mini AX200, KETIANJIAN PHOTOELECTRICITY). The onset of ultrasonic actuation was defined as t = 0. Bead distributions were collected at 0, 25, 60, and 120 frames for each incidence-angle condition.

2.5 Nucleic acid extraction experiment

Human cytomegalovirus (HCMV) was used as the target virus to evaluate nucleic acid extraction performance. To assess extraction in a complex biological matrix, HCMV samples were spiked into fetal bovine serum (FBS) before extraction. The initial HCMV concentration was 8.65×10^4 copies/mL. Ultrasound-assisted extraction was performed at incidence angles of 0°, 10°, 20°, and 30° using the six-degree-of-freedom platform. Each ultrasound-assisted lysis step lasted 10 s. The reagent volumes used for magnetic bead-based extraction are listed in Table 1. During lysis, magnetic beads, HCMV sample, and lysis buffer were mixed to a total reaction volume of 205 μL. Ultrasound was applied only during the lysis step. Magnetic separation, washing, elution, and qPCR amplification were kept identical to those in the standard manual extraction method, so that intergroup differences mainly reflected the lysis and bead-dispersion stages. Three independent extractions were performed for each condition, and each extract was analyzed in technical triplicate by qPCR.

The standard manual extraction method was used as the reference method. Lysis buffer, magnetic beads, and HCMV-spiked FBS samples were mixed according to the reagent protocol, followed by vortex-assisted lysis for 5 min. After lysis, the tube was placed on a magnetic separator, and the supernatant was removed after complete bead capture. Wash Buffer 1 and Wash Buffer 2 were then added sequentially, vortexed for 30 s, and removed after magnetic separation. The beads were subsequently washed twice with DEPC-treated water. Finally, elution buffer was added, the mixture was vortexed for 4 min, magnetic separation was performed, and the supernatant was collected as the extracted nucleic acid product.

Table 1
Reagent volumes used for magnetic bead-based HCMV nucleic acid extraction

Reagent	Volume
Magnetic beads	15 μL
CMV sample	80 μL
Lysis buffer	110 μL
Wash buffer 1	200 μL
Wash buffer 2	200 μL
Wash buffer 3 (DEPC water)	300 μL
Elution buffer	80 μL

2.6 qPCR detection

Extracted HCMV nucleic acids were quantified by real-time quantitative PCR (qPCR). Each 40 μL reaction contained 5 μL of extracted product, 0.4 μL of Takara Taq Hot Start Version (Takara, Japan), 4 μL of 2.5

mM dNTP mixture (Takara, Japan), 4 μL of 10× PCR buffer (Mg^{2+} plus, Takara, Japan), 1 μL of forward primer, 1 μL of reverse primer, 1 μL of TaqMan probe, and 23.6 μL of DEPC-treated water. Amplification was performed on a Bio-Rad CFX96 Touch Real-Time PCR System. The qPCR program was as follows: reverse transcription at 50°C for 3 min, pre-denaturation at 95°C for 2 min, and 45 amplification cycles of denaturation at 95°C for 5 s and annealing/extension at 55°C for 10 s.

2.7 Quantitative metrics and statistical analysis

The descriptors were assigned physical interpretations before their scoring directions were specified. Centroid displacement measures the net migration of the bead-population centroid from its initial position. Greater displacement may indicate transport into different regions, but can also result from coherent motion of a compact bead population. Internal RMS quantifies displacement relative to the population centroid and therefore distinguishes internal rearrangement from collective translation. The bottom escape fraction quantifies the instantaneous fraction of beads outside the defined bottom region, while bead coverage measures the occupied fraction of the analysis grid. Together, these descriptors distinguish population migration, relative motion, and spatial access. Such changes may increase opportunities for bead–target encounters, but neither encounter frequency nor the fraction of nucleic acids contacting beads was calculated in this model. At the specified sampling interval, JSD measures the magnitude of change between consecutive spatial distributions; it does not directly measure mixing uniformity or a kinetic rate constant. Redistribution efficiency describes the fraction of total mean-squared displacement attributable to internal rearrangement, rather than the speed of redistribution. Late-stage directionality measures the alignment of bead displacement vectors. Lower directionality indicates less coherent alignment, but does not by itself demonstrate circulation, dispersion, or better mixing. Flow intensity, coverage, local rotation, and speed uniformity provide complementary descriptions of the fluid motion driving these particle-transport patterns.

The flow index was the equal-weight mean of the five normalized flow descriptors. The bead transport index averaged seven normalized descriptors: early JSD, internal RMS, redistribution efficiency, centroid displacement, late-stage directionality, bottom escape fraction, and bead coverage. Except for early JSD and late-stage directionality, these bead descriptors were evaluated at 10 s. Late-stage directionality was averaged over the eight 1-s intervals spanning 2–10 s. Centroid displacement was positively normalized to represent the extent of net population migration, considered jointly with internal rearrangement and spatial coverage. Late-stage directionality remained reverse-normalized to assign higher scores to less coherently aligned motion. All other descriptors were positively normalized. These scoring directions specify transport preferences within the index; they do not establish that maximizing each positively scored quantity improves extraction. Normalized values describe relative positions among the four configurations, and zero does not necessarily indicate the absence of the corresponding physical process.

The composite transport score was the arithmetic mean of the flow index, bead transport index, positively normalized centroid displacement at 10 s, and normalized bottom escape fraction at 10 s. Centroid displacement was positively normalized both within the bead transport index and as a separate

component of the composite score. Because centroid displacement and bottom escape also entered the bead transport index, each retained an effective weight of 2/7 in the composite score. All other weights were unchanged. The score contains no qPCR measurement, but its revised scoring direction was considered during retrospective interpretation of this dataset. It was therefore treated as a descriptive summary rather than an independently validated predictor. The original and revised scores were compared as a sensitivity analysis. Detailed definitions, normalization procedures, and effective weights are provided in the **Supplementary Material**.

Ct values were used to compare qPCR responses following extraction. Each condition comprised three independent extractions, with three technical qPCR replicates per extraction. Technical replicate Ct values were averaged within each extraction. Group means and sample standard deviations were calculated from the three extraction means, giving an independent sample size of n = 3 per condition. The Ct-based coefficient of variation was calculated as the extraction-level SD divided by the group mean Ct, multiplied by 100%.

ΔCt was defined as the mean Ct for manual extraction minus the mean Ct for the corresponding ultrasound-assisted condition. A positive ΔCt therefore indicated a lower mean Ct than the manual reference. Relative target yield was estimated as $2^{\Delta Ct}$, with manual extraction set to 1, assuming 100% amplification efficiency. This estimate described relative amplifiable target amounts under comparable amplification conditions and was not an absolute extraction recovery rate.

Group comparisons used two-sided Welch t-tests on extraction means, with Holm adjustment across seven comparisons. These comprised each ultrasound-assisted condition versus manual extraction and 10° versus 0°, 20°, and 30°. Adjusted $P < 0.05$ was considered statistically significant. Exploratory Pearson correlations used group-mean ΔCt and simulated descriptors or indices across the four incidence-angle conditions. Correlations for individual descriptors used their original physical values, including centroid displacement and directionality, rather than their normalized scores. Correlations for the bead transport index and composite score were recalculated using the revised positive-centroid formulation. These four-condition correlations were descriptive and were not used to validate a predictive model.

3. Results and Discussion

3.1 Acoustic pressure field distribution

Figure 2 shows the frequency-domain acoustic pressure simulations performed at different incidence angles to evaluate how transducer orientation affected the acoustic response of the reaction chamber. Figure 2a and Fig. 2b show the acoustic pressure distributions from two viewing directions. Because the normal vector of the transducer end face was directed toward the geometric center of the spherical cavity, pressure values were extracted along the path from the transducer-chamber contact point to the cavity center.

The incidence angle markedly affected the position, spatial extent, and gradient of the high-pressure regions within the chamber. Compared with the 0°, 20°, and 30° configurations, the 10° configuration produced stronger pressure variation in the central cavity and more pronounced local gradients near the source-affected region. Quantitative analysis showed that the peak acoustic pressure at 10° was approximately 1.2×10^6 Pa, about 50% higher than that at 0° and about 100% higher than that at 30°. These results show that changing the coupling orientation altered both the magnitude and spatial distribution of the simulated acoustic pressure under the same nominal driving conditions. We therefore examined how these acoustic-field differences were accompanied by changes in streaming and its spatial coverage within the chamber.

3.2 Acoustic streaming configuration

We next examined the spatial distribution and coverage of acoustic streaming within the chamber, using local and mean velocities as complementary measures of flow intensity. Figure 3a-3d show the acoustic streaming distributions at the four incidence angles. At 0°, a localized high-velocity flow developed near the contact zone at the bottom of the chamber, with a peak velocity of approximately 337 mm/s. The flow field mainly formed a localized circulation pattern that originated from the lower region and extended into the chamber interior. This pattern indicates that the 0° configuration generated strong local actuation, but the high-velocity region remained concentrated near the bottom and had a limited chamber-wide effect. When the incidence angle was changed to 10°, the streaming topology changed substantially. Although the peak velocity at 10° was approximately 160 mm/s, lower than the peak value at 0°, the recirculating region expanded markedly and formed a more continuous chamber-scale streaming pattern. At 20° and 30°, the peak velocities decreased to approximately 101 and 42.7 mm/s, respectively, and the circulation regions were more restricted.

The quantitative plots in Fig. 3e–h characterize complementary aspects of streaming intensity and spatial coverage. Figure 3e compares mean flow speed, which was highest at 10°, approximately 0.017 mm/s, compared with 0.0067, 0.0073, and 0.0016 mm/s at 0°, 20°, and 30°, respectively. Figure 3f compares flow coverage area, defined as the area within the analysis domain where speed exceeded the specified threshold. This area reached 25.2 mm^2 at 10°, compared with 9.8, 8.5, and 1.2 mm^2 at 0°, 20°, and 30°, respectively. Figure 3g compares mean vorticity magnitude, which characterizes local fluid rotation. The value was highest at 10°, approximately 0.037 s^{-1}, compared with 0.021, 0.014, and 0.0048 s^{-1} at the other three angles, respectively. Figure 3h summarizes five normalized flow descriptors and their equal-weight flow index, allowing flow intensity, spatial coverage, rotation, and speed uniformity to be considered together. The flow indices were 0.49, 0.88, 0.37, and 0.00 at 0°, 10°, 20°, and 30°, respectively. A zero index indicates the lowest normalized component values within the tested set, rather than the absence of flow. Together, these results distinguish strong localized actuation from more spatially extensive streaming: 0° produced the highest local peak velocity, whereas 10° combined a higher mean speed with broader flow coverage. We next examined whether these distinct simulated flow conditions were accompanied by differences in bead escape from the bottom region and internal rearrangement.

3.3 Magnetic bead redistribution under different streaming configurations

Figure 4. Simulated magnetic bead redistribution under acoustic actuation. (a–d) Spatial bead distributions at 0, 1, 2, and 5 s for incidence angles of 0°, 10°, 20°, and 30°, respectively. (e) JSD between consecutive spatial distributions at 1-s intervals over 0–10 s. (f) Centroid-displacement–internal-RMS trajectories over 0–10 s; the endpoint of each trajectory corresponds to 10 s. (g) Heatmap of seven normalized bead-transport descriptors and their equal-weight bead transport index. The descriptors are early JSD, internal RMS, redistribution efficiency, centroid displacement, late-stage directionality, bottom escape fraction, and bead coverage. Centroid displacement is positively normalized; only late-stage directionality is reverse-normalized. Early JSD averages the 0–1 s and 1–2 s intervals, and late-stage directionality averages the eight intervals spanning 2–10 s. The other bead descriptors are evaluated at 10 s. Colors and numerical labels show relative normalized values across the four configurations, not extraction efficiencies.

Monte Carlo particle-trajectory simulations were used to compare magnetic bead dispersion, rearrangement, and spatial accumulation across the four acoustic configurations. The four incidence-angle configurations produced distinct bead-transport profiles. The simulated bead-transport profiles were examined alongside the corresponding streaming fields to relate particle redistribution to the modeled acoustic and flow conditions.

Figure 4a-4d show markedly different bead transport characteristics among the four incidence angles. At 0°, the beads mainly underwent resuspension and movement near the left side of the chamber bottom and within the local circulation zone. At 10°, the bead movement range increased markedly, allowing the beads to travel along a broader circulation path and undergo stronger spatial dispersion and internal rearrangement. At 20°, bead migration was observed, but the distribution range was smaller than that at 10° and remained mainly localized near the initial actuation region. At 30°, bead transport was the weakest, with most beads remaining near the bottom or in localized clusters.

The JSD time course in **Fig. 4e** distinguishes the magnitude and temporal persistence of distributional changes. The 20° configuration exhibited the largest peak, 0.6645 during 1–2 s, and the highest mean adjacent-step JSD over both 0–2 s and 0–10 s. The respective means were 0.5133 and 0.14237 at 20°, compared with 0.2666 and 0.07186 at 10°. The 10° configuration showed a larger initial response during 0–1 s and higher JSD in each interval from 4 to 10 s. Over 5–10 s, mean adjacent-step JSD was 0.01385 at 10° and 0.00408 at 20°. Thus, 20° produced larger early distributional changes, whereas 10° maintained greater late-stage changes. JSD measures differences between spatial distributions; it does not establish whether those distributions become more uniform or improve extraction. The temporal profiles were therefore interpreted alongside displacement, internal RMS, bottom escape fraction, and bead coverage, without assigning an extraction ranking from JSD alone.

The centroid-displacement–internal-RMS trajectories in **Fig. 4f** distinguish overall bead migration from motion within the bead population. At 10 s, centroid displacement and internal RMS were 1.50 and 2.05 mm at 10°, compared with 0.099 and 1.16 mm at 0°. The corresponding values were 0.741 and 1.24 mm at 20°, and 0.438 and 0.605 mm at 30°. The small centroid displacement at 0° therefore did not indicate an absence of bead motion: substantial motion occurred relative to the population center. In contrast, 10° combined greater population migration with a larger magnitude of internal motion. This distinction is relevant in a confined chamber, where the displacement of the population center alone cannot describe the motion occurring within the bead population. Together with the higher bottom escape fraction and broader bead coverage at 10°, these results indicate that internal motion was accompanied by redistribution beyond the initial bottom region. They characterize complementary aspects of simulated transport rather than directly measuring molecular mixing or nucleic acid adsorption.

The bead-transport heatmap in **Fig. 4g** summarizes seven normalized descriptors and their equal-weight index. With centroid displacement positively normalized, the bead transport indices were 0.428, 0.751, 0.502, and 0.037 at 0°, 10°, 20°, and 30°, respectively. The 10° configuration had the highest centroid displacement, internal RMS, bottom escape fraction, and bead coverage, whereas 20° had the highest mean early JSD. At 10 s, the fractions outside the bottom region were 28.7%, 68.0%, 39.4%, and 0.0% at 0°, 10°, 20°, and 30°, respectively. These original fractions differ from the normalized scores in the heatmap. The zero normalized centroid score at 0° indicates the smallest displacement among the tested configurations, not an absence of bead motion. The index summarizes the selected transport preferences, while the component profiles and temporal trajectories retain differences that cannot be represented by a single score.

The image sequences in Fig. 5 provided a qualitative comparison with the simulated redistribution patterns. At 10°, beads moved from the bottom region into a broader portion of the chamber interior. Motion at 0° remained more localized, while redistribution at 20° and 30° appeared more restricted. These observations provided qualitative context rather than quantitative validation of the simulated velocities or transport descriptors.

Taken together, the simulations characterized 10° by broader flow coverage, greater internal motion, and a higher bottom escape fraction. Its distributional changes also persisted later during actuation, whereas 20° showed the largest early JSD. The descriptors therefore identified distinct transport profiles rather than a uniform ranking. These profiles provided the physical basis for examining whether the configurations also differed in experimental extraction outcomes.

3.4 Extraction performance and its relationship with bead transport

Extraction performance was compared across the same four configurations using qPCR measurements following extraction from HCMV-spiked fetal bovine serum. This comparison examined whether the simulated transport differences were accompanied by differences in the experimental endpoint.

The Ct panel in Fig. 6a shows individual qPCR measurements, extraction means, and group mean ± SD. Manual extraction yielded a mean Ct of 31.87 ± 0.27. Mean Ct values at 0°, 10°, 20°, and 30° were 31.38 ± 0.19, 30.86 ± 0.28, 31.07 ± 0.51, and 31.41 ± 0.11, respectively. The corresponding qPCR amplification curves, including extraction blanks and no-template controls, are provided in **Fig. S1**. Each group comprised three independent extractions, with technical triplicates averaged within each extraction. The lowest mean Ct was observed at 10°, with a reduction of 1.01 cycles relative to manual extraction. This corresponded to an estimated relative target yield of 2.02 under the assumption of 100% qPCR amplification efficiency. The numerical summary is provided in Table 2. None of the seven specified comparisons reached adjusted $P < 0.05$ after Holm correction of two-sided Welch tests. The mean ordering therefore describes the present dataset without establishing a statistically confirmed optimum. No amplification was observed in extraction blanks or no-template controls.

Table 2
Summary of qPCR responses following manual and ultrasound-assisted extraction

Condition	Mean Ct ± SD	Ct-based CV (%)	ΔCt versus manual extraction	Estimated relative target yield, manual = 1
Manual extraction	31.87 ± 0.27	0.72	0	1.000
0°	31.38 ± 0.19	0.61	0.49	1.401
10°	30.86 ± 0.28	0.94	1.01	2.015
20°	31.07 ± 0.51	1.58	0.80	1.746
30°	31.41 ± 0.11	0.35	0.46	1.377

The transport-profile heatmap in Fig. 6b compares the component profiles and revised summary scores. With centroid displacement positively normalized in both the bead index and the separate composite component, composite scores were 0.3342, 0.9076, 0.4783, and 0.0696 at 0°, 10°, 20°, and 30°, respectively. The 10° configuration combined broader flow coverage, greater net bead migration, greater internal rearrangement, and a higher bottom escape fraction. Its highest score coincided with the lowest observed mean Ct, although it did not have the highest peak flow speed or mean early JSD. The score ordering matched the numerical ordering of mean Ct, but the different scores at 0° and 30° contrasted with their nearly identical mean Ct values. Changing the centroid scoring direction also substantially altered the scores and reversed the relative positions of 0° and 20°. This sensitivity shows why component profiles and temporal trajectories remain necessary for interpretation. The flow–bead transport map in Fig. 6d summarizes the revised indices and mean Ct values without providing an independent test of extraction superiority.

The exploratory correlation plot in Fig. 6c compares all simulated transport descriptors and summary indices with group-mean ΔCt across four configurations. Flow-field uniformity showed r = 0.99, followed by centroid displacement at 0.94 and bottom escape fraction at 0.91. Internal RMS and mean flow speed each showed r = 0.89. Bead coverage, flow coverage area, and mean vorticity magnitude showed r = 0.87, 0.85, and 0.74, respectively. Early JSD showed r = 0.44, whereas peak flow speed, redistribution efficiency, and late-stage directionality showed r = − 0.16, − 0.48, and − 0.55. The flow index, bead transport index, and composite transport score showed r = 0.78, 0.86, and 0.94, respectively. For individual descriptors, correlations used original physical values rather than normalized scores. The bead-index and composite-score correlations were recalculated after changing centroid displacement to positive normalization. Their increased correlations do not provide independent validation of the revised scoring convention. With only four configurations, the coefficients describe associations within this dataset and cannot establish descriptor importance, causal effects, or predictive performance. They complement the physical interpretation but do not provide independent validation of it.

A possible transport-based explanation involves the combination of spatial access and motion within the bead population. Broader streaming coverage can extend the region in which beads are mobilized, while a higher bottom escape fraction and greater bead coverage indicate redistribution beyond the initial accumulation region. Internal RMS adds a different dimension by quantifying motion that remains after collective translation is removed. When these features occur together, beads may have more opportunities to encounter released nucleic acids distributed across the reaction volume. However, bead displacement alone does not establish renewal of the liquid surrounding each bead, because beads and liquid may move together. Improved capture would depend on relative transport between targets and bead surfaces, as well as the binding conditions. The present descriptors therefore provide a physical basis for a hypothesis of increased encounter opportunities, rather than a direct measurement of contact frequency, adsorption kinetics, or capture efficiency.

The correspondence between simulated transport and extraction outcomes was incomplete. Despite different transport profiles, 0° and 30° yielded similar mean Ct values, 31.38 and 31.41, respectively. The 10° and 20° configurations also differed in transport characteristics, but their mean Ct difference did not reach statistical significance. Similar means or nonsignificant differences do not establish equivalence between configurations. The transport descriptors characterize fluid and bead motion rather than directly measuring nucleic acid release, bead–target contact, or binding kinetics. The qPCR endpoint reflects the combined effects of target release, capture, and residual amplification inhibition. Moreover, changing coupling orientation altered acoustic pressure as well as streaming, so the contribution of streaming configuration was not independently isolated. Simulations using a simplified fluid medium and qualitative imaging therefore provide a transport interpretation whose causal contributions remain unresolved.

For the present chamber, configuration assessment should consider both the spatial reach of bead transport and the magnitude of motion within the bead population. Broad streaming coverage and mobilization beyond the bottom region describe where transport occurs, whereas internal RMS

describes the magnitude of motion after collective translation is removed. Centroid displacement and bead coverage provide complementary information on population relocation and spatial distribution. A candidate configuration should therefore combine these features rather than maximize any single displacement or intensity measure. The 10° configuration exhibited this combination and had the lowest observed mean Ct under the tested conditions. This observation does not establish statistically significant extraction superiority or a universal optimum. Incidence angle should therefore be viewed as a control variable for generating transport states, while configuration assessment should retain multi-descriptor characterization and joint interpretation. Application to other chamber geometries, sample volumes, and matrices requires further evaluation.

4. Conclusion

This study combined computational characterization of acoustic streaming and magnetic bead transport with experimental comparisons of nucleic acid extraction in a closed chamber. The analysis distinguished local flow intensity from spatial coverage, overall bead migration from internal motion, and early distributional changes from persistent late-stage redistribution. The 10° configuration combined broader flow coverage, greater internal rearrangement, and a higher bottom escape fraction, whereas 20° exhibited the highest mean early JSD. The lowest mean Ct was observed at 10°, although group differences did not reach statistical significance after Holm adjustment. Similar mean Ct values at 0° and 30° also indicated that transport differences did not fully account for extraction outcomes. Together, these findings provide a transport-based assessment framework connecting acoustic streaming configuration, bead transport, and extraction response. For the present chamber, broad streaming coverage, mobilization of bottom-region beads, and internal rearrangement during overall migration constitute complementary candidate design criteria. The persistence of redistribution provides an additional temporal consideration. By retaining these complementary features, the framework provides a basis for comparing configurations and identifying candidate designs for ultrasound-assisted magnetic bead extraction.

Declarations

The authors have no conflict of interest.

Funding

This work was supported in part by National Natural Science Foundation of China (No.62472365), in part by Natural Science Foundation of Xiamen Municipality (No.3502Z202473003), in part by Special Fund for Central Government-Guided Local Science and Technology Development of Xinjiang (No. ZYYD2026QY25), in part by the Science and Technology Major Project of Inner Mongolia Autonomous Region (No. 2025YFDZ0108).

Author Contribution

Yuan Qian: conceptualization, methodology, simulation, formal analysis, writing—original draft; Jiayu Yang: conceptualization, methodology, visualization, data analysis; Lili Pan: resource; Ran An: resource; Zhuolun Li: software; Yuhong Yang: data curation; Junnan Wang: data curation; Lin Xiao: software; Tiesheng Zheng: supervision, resources; Ningshao Xia: supervision, resources; Fa Zhang: supervision; Lijie Yuan: supervision; Dongxu Zhang: conceptualization, project administration, funding acquisition. All authors reviewed and approved the final manuscript.

Data Availability

Data will be made available on request.

References

1. Cai S, Jin Y, Lin Y, He Y-Z, Zhang P, Ge Z, Yang W (2023) Micromixing within microfluidic devices: Fundamentals, design, and fabrication. Biomicrofluidics 17(6):61503. https://doi.org/10.1063/5.0178396
2. Noroozi Z, Kido H, Mićić M, Pan H, Bartolome C, Princevac M, Zoval J, Madou M (2009) Reciprocating flow-based centrifugal microfluidics mixer. Rev Sci Instrum 80(7):75102. https://doi.org/10.1063/1.3169508
3. Suh Y, Kang S-M (2010) A Review on Mixing in Microfluidics, Micromachines 1. 82–111. https://doi.org/10.3390/mi1030082
4. Kundu D, Roy S, Bhattacharjee S, Saha S, Chakrabarty K, Chakrabarti P, Bhattacharya B (2022) Mixing Models as Integer Factorization: A Key to Sample Preparation With Microfluidic Biochips. IEEE Trans Comput Aided Des Integr Circuits Syst 41:558–570. https://doi.org/10.1109/tcad.2021.3063342
5. Liang T-C, Chan Y-S, Ho T-Y, Chakrabarty K, Lee C-Y (2020) Multitarget Sample Preparation Using MEDA Biochips. IEEE Trans Comput Aided Des Integr Circuits Syst 39:2682–2695. https://doi.org/10.1109/tcad.2019.2942002
6. Nguyen N, Hejazian M, Ooi C, Kashaninejad N (2017) Recent Advances and Future Perspectives on Microfluidic Liquid Handling, Micromachines 8. https://doi.org/10.3390/mi8060186
7. Lee C-Y, Chang C, Wang Y-N, Fu L-M, Mixing M (2011) A Review, International Journal of Molecular Sciences 12, 3263–3287. https://doi.org/10.3390/ijms12053263
8. Lee C-Y, Wang W-T, Liu C-C, Fu L-M (2016) Passive mixers in microfluidic systems: A review. Chem Eng J 288:146–160. https://doi.org/10.1016/j.cej.2015.10.122
9. Zhang K-L, Ren Y, Hou L, Tao Y, Liu W, Jiang T, Jiang H-Y (2019) Continuous microfluidic mixing and the highly controlled nanoparticle synthesis using direct current-induced thermal buoyancy convection. Microfluid Nanofluid 24. https://doi.org/10.1007/s10404-019-2306-y

10. Ge M, Chen J, Zhao L, Zheng G (2023) Mixing Transport Mechanism of Three-Phase Particle Flow Based on CFD-DEM Coupling. https://doi.org/10.3390/pr11061619
11. González-Lavín G, García-Merino B, Fernández-Maza C, Bringas E, Gómez-Coma L, Fallanza M, Ortiz I (2024) Tailored Euler-Lagrange modelling of microfluidic Solid/Liquid reactive separations. Chem Eng J. https://doi.org/10.1016/j.cej.2024.153393
12. Sun L, Siddique M, Wang L, Li S (2021) Mixing characteristics of a bubble mixing microfluidic chip for genomic DNA extraction based on magnetophoresis: CFD simulation and experiment, ELECTROPHORESIS 42. https://doi.org/10.1002/elps.202000295
13. Gao Y-H, Zhu D-F-N-CK-T, Han Y, Torrente-Murciano L (2021) Rational design of the inlet configuration of flow systems for enhanced mixing. J Flow Chem 11:589–598. https://doi.org/10.1007/s41981-021-00184-z
14. Hoffmann M, Schlüter M, Räbiger N (2006) Experimental investigation of liquid–liquid mixing in T-shaped micro-mixers using μ-LIF and μ-PIV. Chem Eng Sci 61:2968–2976. https://doi.org/10.1016/j.ces.2005.11.029
15. Lu Y, Tan W, Mu S, Zhu G (2024) Vortex-Enhanced Microfluidic Chip for Efficient Mixing and Particle Capturing Combining Acoustics with Inertia. Anal Chem. https://doi.org/10.1021/acs.analchem.3c05291
16. Jue E, Witters D, Ismagilov R (2020) Two-phase wash to solve the ubiquitous contaminant-carryover problem in commercial nucleic-acid extraction kits. Sci Rep 10. https://doi.org/10.1038/s41598-020-58586-3
17. Howard R, Roque S, Kamineni P, Davis E, Anfora A, Konigshofer Y, Huang C, Garlick R (2026) Abstract 3261: Evaluation of FFPE-extracted nucleic acid quality and performance from various commercial extraction kits using contrived multiplexed reference materials. Cancer Res. https://doi.org/10.1158/1538-7445.am2026-3261
18. Dubinsky A, Saunders L, Abstract (2021) 2281: Impact of DNA contaminants on next-generation sequencing data quality, Molecular and Cellular Biology/Genetics https://doi.org/10.1158/1538-7445.am2021-2281
19. Wu M, Huang Y-H, Huang Y-R, Wang H, Li M, Zhou Y, Zhao H, Lan Y, Wu Z, Jia C-P et al (2023) Droplet magnetic-controlled microfluidic chip integrated nucleic acid extraction and amplification for the detection of pathogens and tumor mutation sites. Anal Chim Acta 1271:341469. https://doi.org/10.1016/j.aca.2023.341469
20. Fan Y, Dai R, Guan X, Lu S-Y, Yang C-H, Lv X-F, Li X (2023) Rapid Automatic Nucleic Acid Purification System Based on Gas-Liquid Immiscible Phase. J Sep Sci. https://doi.org/10.1002/jssc.202200801
21. Stringer M, Zeng Z, Zhang X, Chai Y, Li W, Zhang J-K, Ong H, Liang D, Dong J, Li Y-M et al (2023) Methodologies, technologies, and strategies for acoustic streaming-based acoustofluidics. Appl Phys Reviews. https://doi.org/10.1063/5.0134646
22. Pavlic A, Harshbarger C, Rosenthaler L, Snedeker J, Dual J (2022) Sharp-edge-based acoustofluidic chip capable of programmable pumping, mixing, cell focusing and trapping. Phys Fluids.

https://doi.org/10.1063/5.0133992

23. Das PK, Meinhart C, Tenje M (2026) Acoustic streaming and shape evolution of viscous droplets in ultrasonic fields. J Fluid Mech 1036. https://doi.org/10.1017/jfm.2026.11649
24. Bruus H (2012) Acoustofluidics 7: The acoustic radiation force on small particles, Lab on a chip 12 6. 1014–1021. https://doi.org/10.1039/c2lc21068a
25. Muller P, Barnkob R, Jensen M, Bruus H (2012) A numerical study of microparticle acoustophoresis driven by acoustic radiation forces and streaming-induced drag forces, Lab on a chip 12 22. 4617–4627. https://doi.org/10.1039/c2lc40612h
26. Muller P, Bruus H (2015) Theoretical study of time-dependent, ultrasound-induced acoustic streaming in microchannels, Physical review. E, Statistical, nonlinear, and soft matter physics 92 6, 63018. https://doi.org/10.1103/physreve.92.063018
27. Chaichypour B, Jegatheeswaran S, Salari A, Kun D, Kolios M, Tsai S, ACOUSTICALLY EXCITED MICROPOST-BASED, MICROMIXERS: ENHANCING MIXING PERFORMANCE VIA ACOUSTIC MICROSTREAMING USING SYNTHESIZED MICROPOSTS IN MICROFLUIDIC DEVICES (2024), MicroTAS Book of Abstracts (2024). https://doi.org/10.70477/dmay7292
28. Hsu J-C (2025) Enhanced Micromixing Using Surface Acoustic Wave Devices: Fundamentals, Designs, and Applications, Micromachines 16. https://doi.org/10.3390/mi16060619
29. Wu J, Streaming A, Applications I (2018) Fluids https://doi.org/10.3390/fluids3040108
30. Iranmanesh I, Ohlin M, Ramachandraiah H, Ye S, Russom A, Wiklund M (2016) Acoustic micro-vortexing of fluids, particles and cells in disposable microfluidic chips. Biomed Microdevices 18:71. https://doi.org/10.1007/s10544-016-0097-4
31. Li T, You R, Shen X, Li Z, Yang Y, Han Z, Duan X (2025) Reconfigurable acoustic streaming tweezers enabled portable liquid handler for nucleic acid extraction. Ultrason Sonochem 119:107404. https://doi.org/https://doi.org/10.1016/j.ultsonch.2025.107404

Figures

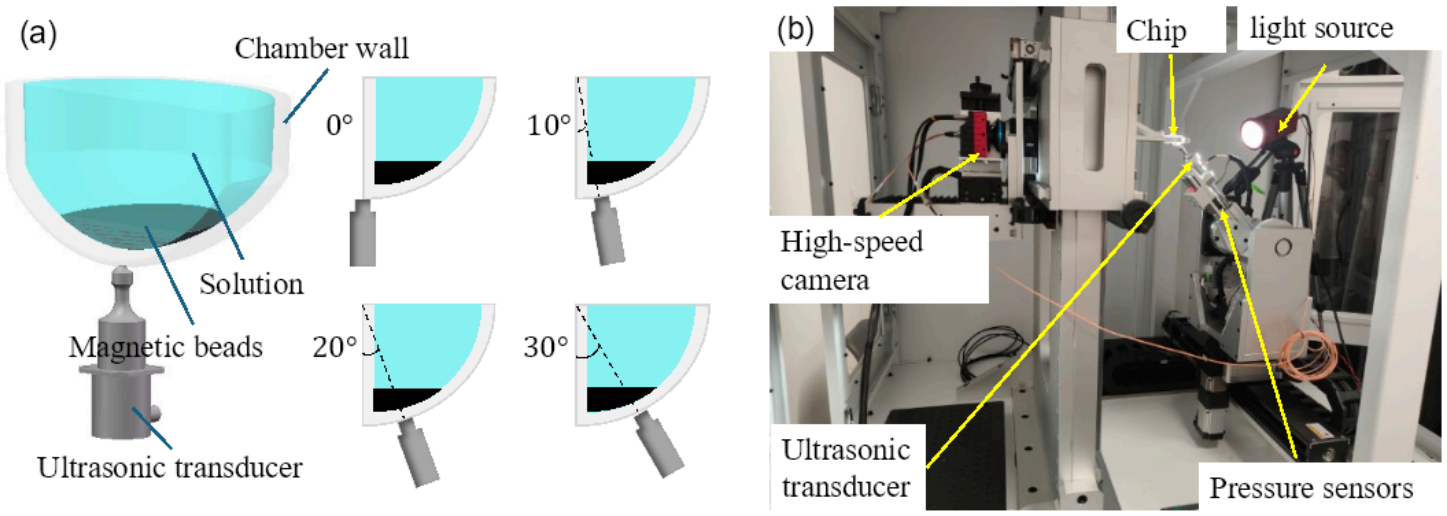


Figure 1

Ultrasound-assisted pretreatment platform with adjustable incidence angle. (a) Schematic of the contact configuration between the ultrasonic transducer and the reaction chamber at different incidence angles. (b) Photograph of the six-degree-of-freedom experimental platform.

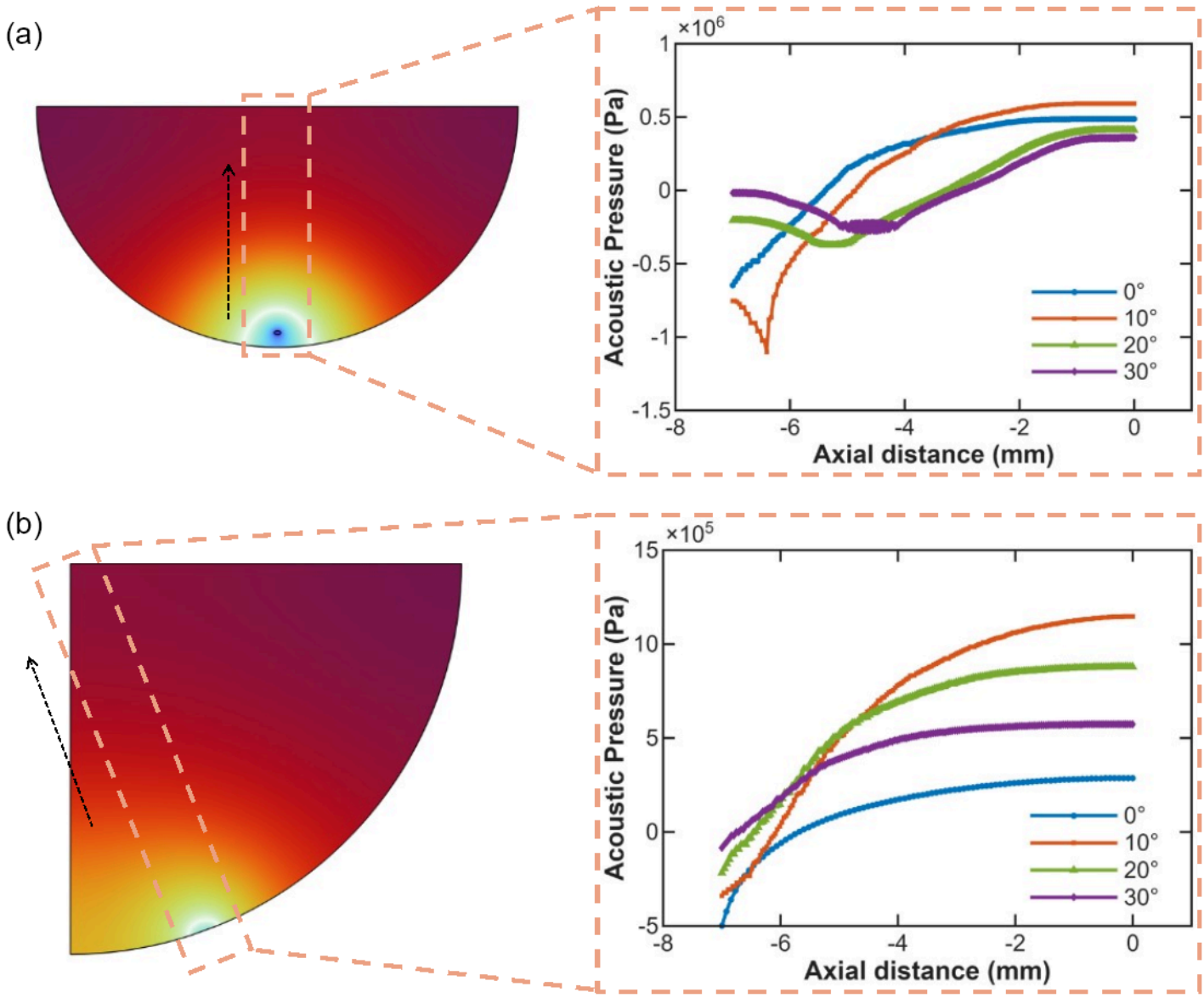


Figure 2

Simulated acoustic pressure distribution in the reaction chamber. (a) Acoustic pressure distribution from viewing direction 1. (b) Acoustic pressure distribution from viewing direction 2. The dashed line indicates the normal direction of the ultrasonic transducer end face.

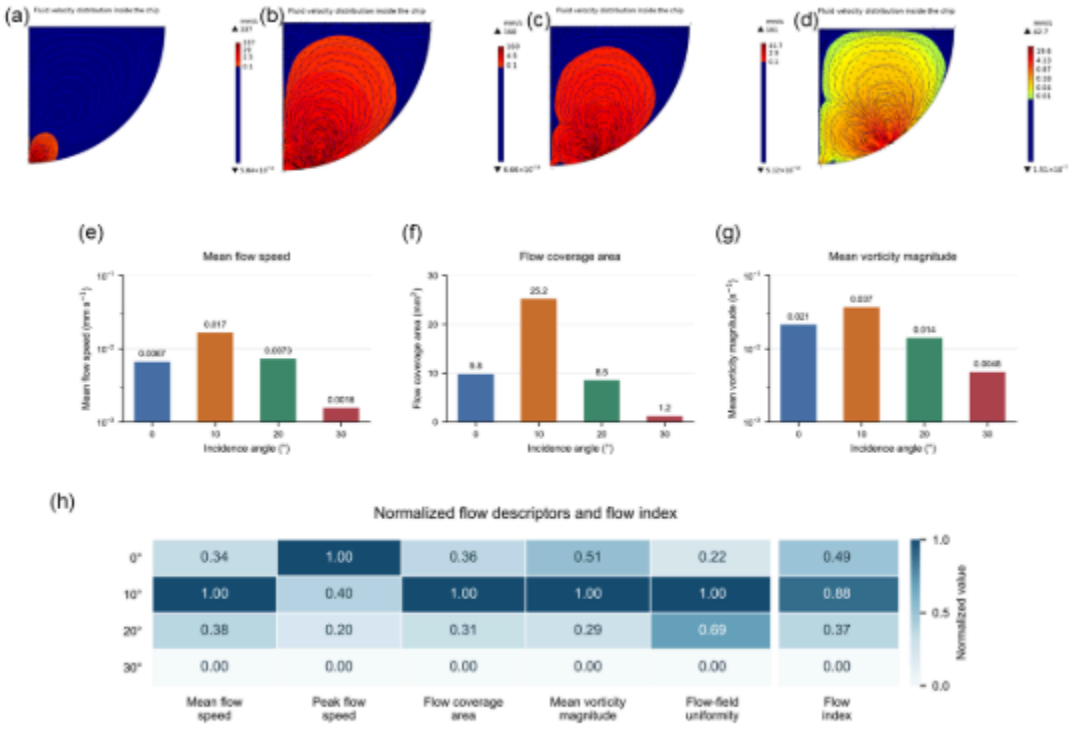


Figure 3

Acoustic streaming fields and quantitative flow characterization at different incidence angles. (a–d) Simulated flow-speed distributions and streamlines at incidence angles of 0°, 10°, 20°, and 30°, respectively. Colors indicate flow speed, and streamlines show the spatial organization of the flow. (e) Mean flow speed. (f) Flow coverage area, defined as the area in the analysis domain where flow speed exceeds the specified threshold. (g) Mean vorticity magnitude. (h) Heatmap of five normalized flow descriptors—mean flow speed, peak flow speed, flow coverage area, mean vorticity magnitude, and flow-field uniformity—and their equal-weight flow index. Normalization was performed across the four configurations. Higher normalized values indicate larger values of the corresponding descriptors; zero denotes the minimum within the tested set rather than the absence of flow. Flow-field uniformity describes the spatial uniformity of speed, not solute concentration.

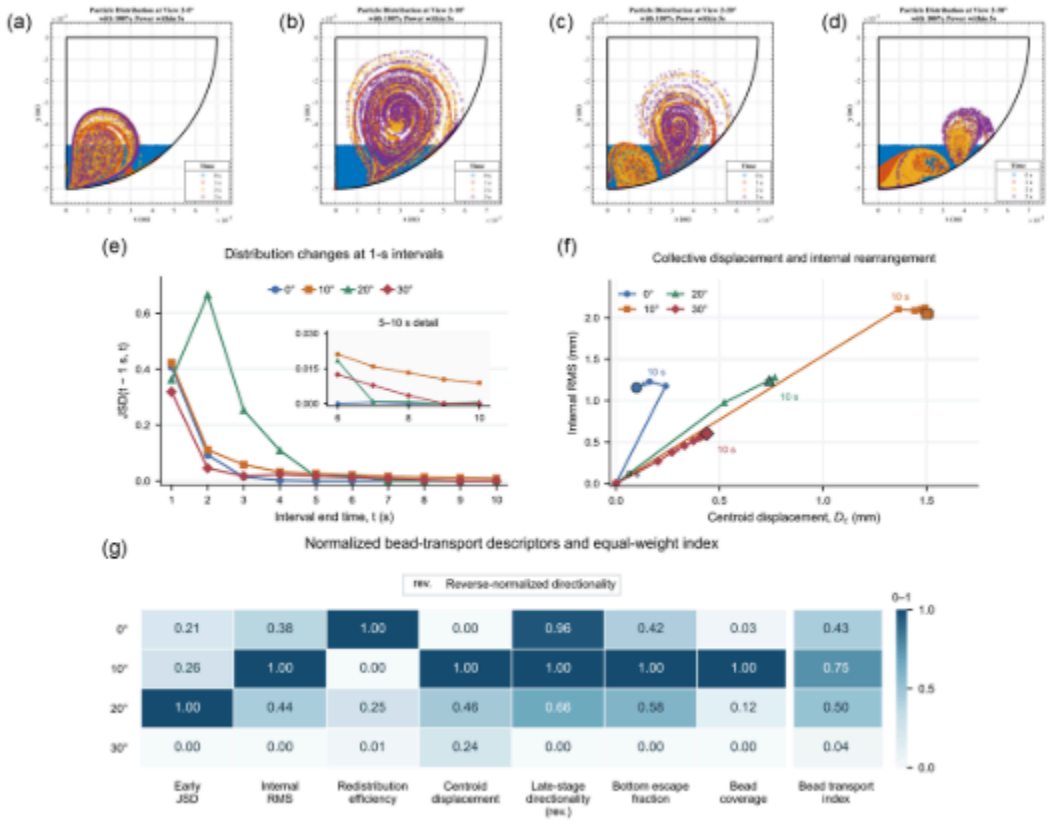


Figure 4

Simulated magnetic bead redistribution under acoustic actuation. (a–d) Spatial bead distributions at 0, 1, 2, and 5 s for incidence angles of 0°, 10°, 20°, and 30°, respectively. (e) JSD between consecutive spatial distributions at 1-s intervals over 0–10 s. (f) Centroid-displacement–internal-RMS trajectories over 0–10 s; the endpoint of each trajectory corresponds to 10 s. (g) Heatmap of seven normalized bead-transport descriptors and their equal-weight bead transport index. The descriptors are early JSD, internal RMS, redistribution efficiency, centroid displacement, late-stage directionality, bottom escape fraction, and bead coverage. Centroid displacement is positively normalized; only late-stage directionality is reverse-normalized. Early JSD averages the 0–1 s and 1–2 s intervals, and late-stage directionality averages the eight intervals spanning 2–10 s. The other bead descriptors are evaluated at 10 s. Colors and numerical labels show relative normalized values across the four configurations, not extraction efficiencies.

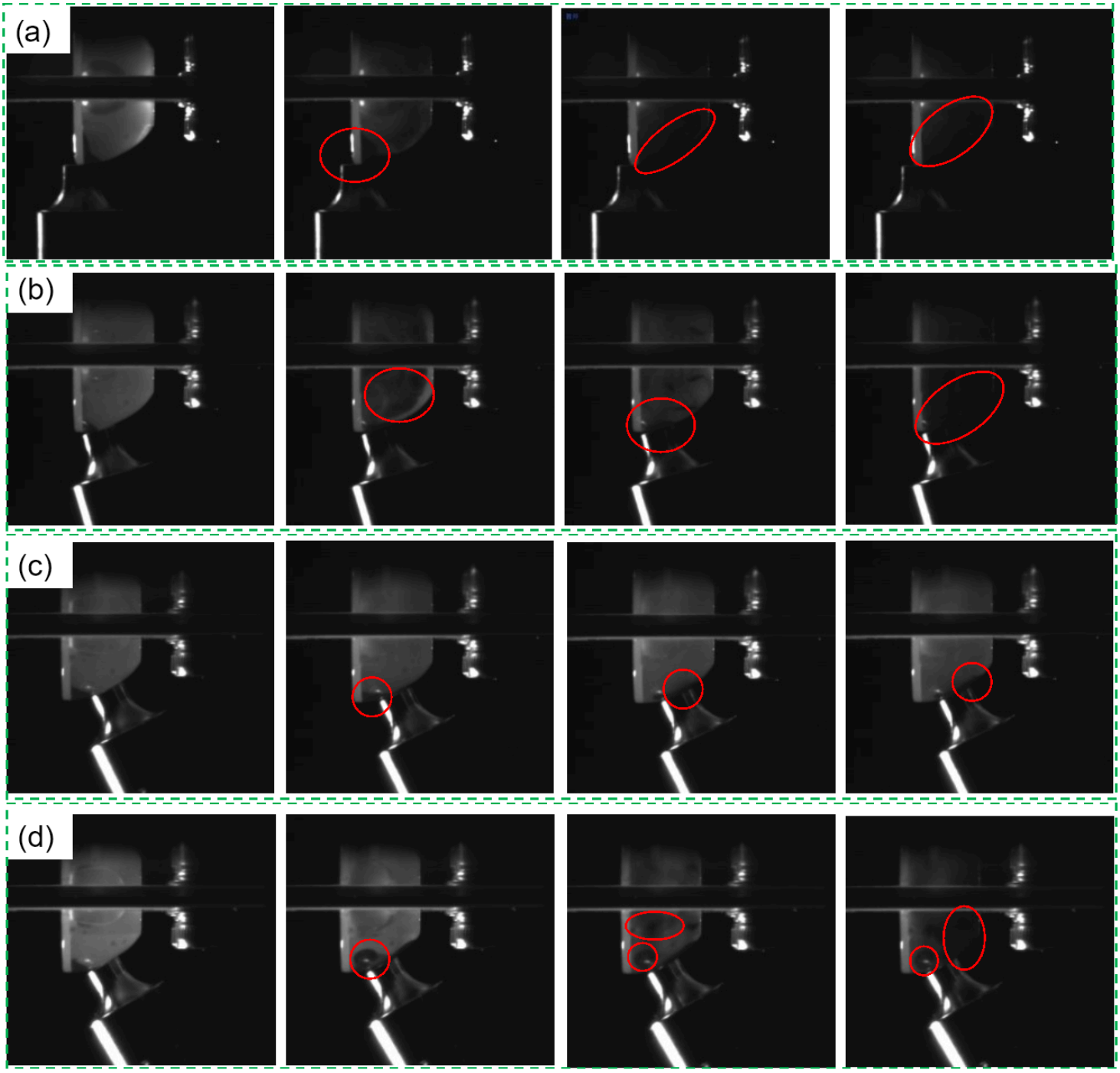


Figure 5

Temporal evolution of magnetic bead distributions during ultrasonic treatment. (a–d) Bead distributions at incidence angles of 0°, 10°, 20°, and 30°, respectively. Red circles highlight selected regions of bead redistribution or localized accumulation.

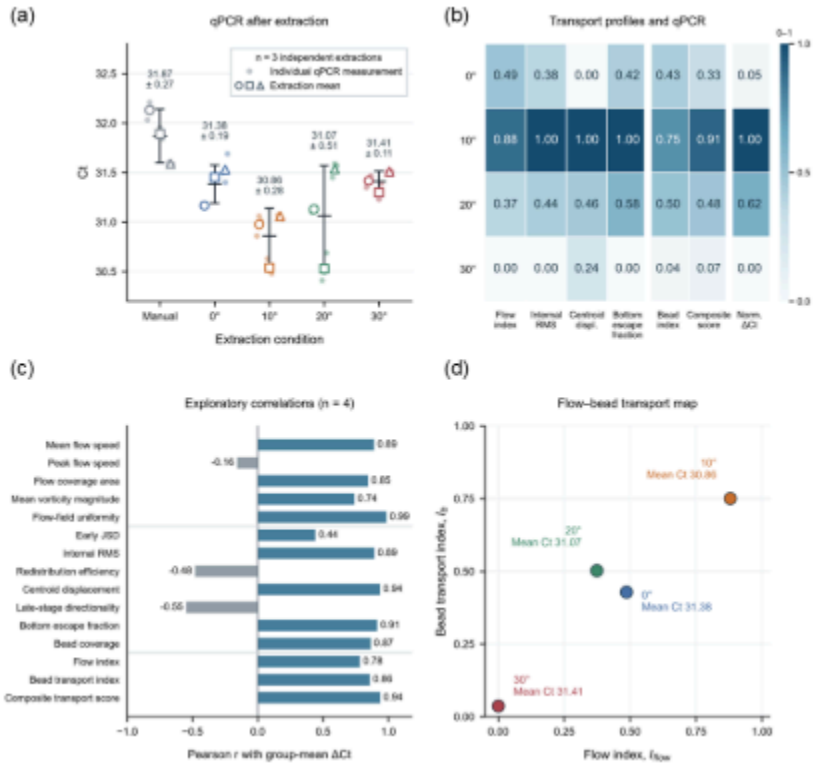


Figure 6

Joint interpretation of simulated transport characteristics and experimental qPCR outcomes. (a) Ct values following manual extraction and ultrasound-assisted extraction at four incidence angles. Light filled circles show individual qPCR measurements from three technical replicates per extraction; open symbols show the mean Ct of each independent extraction. Black horizontal marks and vertical error bars indicate the group mean and sample SD across three independent extractions. Numerical labels give mean ±SD. (b) Heatmap of the flow index, internal RMS, positively normalized centroid displacement, bottom escape fraction, revised bead transport index, revised composite transport score, and normalized group-mean ΔCt. Transport components and ΔCt are displayed on relative 0–1 scales; ΔCt is not included in either transport index. (c) Exploratory Pearson correlations with group-mean ΔCt across four configurations. Individual descriptors use their original physical values, whereas summary indices use the revised scoring formulation. (d) Flow–bead transport map using the flow index and revised bead transport index; labels report the mean Ct for each configuration.

Supplementary Files

This is a list of supplementary files associated with this preprint. Click to download.

- Supplementarymaterial.docx